Flexural buckling behaviour and residual strengths of stainless steel CHS columns after exposure to fire

An He [a], Hai-Ting Li [b], Xiaoyi Lan [c], Yating Liang [d], Ou Zhao *[e]

[a, b, c, e] School of Civil and Environmental Engineering, Nanyang Technological University, Singapore

[d] School of Engineering, University of Glasgow, Glasgow, UK

* Corresponding author, Email: ou.zhao@ntu.edu.sg

Abstract

The flexural buckling behaviour and residual strengths of stainless steel circular hollow section (CHS) columns after exposure to fire were studied, based on a thorough experimental and numerical modelling programme, and reported in this paper. The experimental programme was performed on three series of specimens, and each series contained five geometrically identical specimens, with one unheated and the other four heated to different levels of elevated temperatures (namely 300 °C, 600 °C, 800 °C and 1000 °C). The detailed heating, soaking and cooling processes, material testing and pin-ended column tests were described, with the derived key experimental results fully presented. The testing programme was supplemented by a numerical modelling programme, including a validation study where finite element models were developed and validated against the test results, and a parametric study where the validated finite element models were employed to derive further numerical results over an extended range of cross-section dimensions and member lengths. Due to the absence of existing design codes for stainless steel structures after exposure to fire, the codified design provisions for stainless steel CHS columns at ambient temperature, as established in the Europe, America and Australia/New Zealand, were assessed for their applicability to stainless steel CHS columns after exposure to fire, based on the obtained test and numerical data. The assessment results generally revealed that the design buckling curve, as adopted in the European code, and the tangent modulus method, as employed in the American specification, lead to unsafe and scattered design flexural buckling strengths for stainless steel CHS columns after exposure to fire, while the explicit approach, as used in the Australian/New Zealand standard, yields a high level of accuracy and consistency in predicting the post-fire flexural buckling strengths of stainless steel CHS columns.

Keywords: Circular hollow section (CHS); Design analysis; Flexural buckling behaviour; Heating, soaking and cooling processes; Material tensile coupon tests; Numerical modelling; Pin-ended column tests; Post-fire residual strengths; Stainless steel

1. Introduction

Stainless steel circular hollow sections (CHS) have been increasingly used in civil and offshore engineering, as they uniquely combine the material advantages of stainless steel, including high strength, superior ductility and excellent durability, with the favourable geometric characteristics of circular profiles, including the same cross-section properties in all directions, high torsional stiffness and low drag coefficient. Moreover, stainless steel CHS structural members not only grab the attention of architects and designers, but also attract the interests of researchers, with a brief summary of their previous experimental, numerical and analytical studies provided herein. At cross-sectional level, the local buckling behaviour and compression capacities of stainless steel CHS stub columns were investigated, based on extensive testing programmes [1-9], while the in-plane flexural behaviour and capacities of stainless steel CHS beams were examined through a series of tests [2, 10-12], all indicating that the current design codes yield overly conservative and scattered predictions of cross-section compression and bending moment capacities, due to the use of the 0.2% proof stress as the failure stress in the design without accounting for the pronounced material strain hardening of stainless steel. Zhao et al. [13, 14] experimentally and numerically investigated the local stability and capacities of stainless steel CHS stub columns under combined compression and bending moment, and pointed out the conservatism of the codified cross-section interaction formulations, of which the major shortcoming lies in the neglect of the pronounced material strain hardening effect in the design. Improved design approaches for stainless steel CHS structural components prone to local buckling were then developed by Zhao et al. [14] and Buchanan et al. [15] based on the continuous strength method (CSM) [16-20], and the new proposals account for strain hardening in the predictions of cross-section capacities under both isolated and combined loadings and result in substantially higher levels of design accuracy and consistency than the established codes. At member level, experimental investigations into the flexural buckling behaviour and strengths of stainless steel CHS long columns were carried out and reported in Buchanan et al. [21], where the codified design buckling curves were found to yield inaccurate predictions of flexural buckling strengths and new design buckling curves were also proposed and validated against the experimental data, indicating a higher degree of design accuracy. Zhao et al. [22] and Buchanan et al. [23] conducted thorough experimental and numerical studies of stainless steel CHS long beam-columns, examined their global stability and strengths under combined compression and bending moment, assessed the accuracy of the codified design interaction expressions and finally devised more accurate and efficient design proposals. It is worth noting that the aforementioned previous research efforts focused on the behaviour and capacities of stainless steel CHS structural components at ambient temperature; however, to date, their structural performance and residual strengths in fire and after exposure to fire remain unexplored. A research project has thus been initiated by the authors, aimed at investigating the fire and post-fire performances of various types of stainless steel CHS structural components. The material properties, local buckling behaviour and residual capacities of stainless steel CHS stub columns after exposed to fire has been examined and reported in He et al. [24], while the post-fire flexural buckling behaviour and strengths of stainless steel CHS long columns were investigated in the present study.

In the current work, a testing programme was firstly carried out on three series of stainless steel CHS column specimens, with each series containing five geometrically identical specimens, including one unheated specimen and four specimens heated to different levels of elevated temperatures. A numerical modelling programme was then performed, where finite element models were initially developed to simulate the test post-fire flexural buckling responses and then employed to conduct parametric studies to derive further numerical data over an extended range of cross-section sizes and member lengths. Given that there have been no existing design standards for stainless steel structures after exposure to fire, the flexural buckling design rules for stainless steel CHS columns at ambient temperature, as specified in EN 1993-1-4 [25], SEI/ASCE-8 [26] and AS/NZS 4673 [27], were evaluated for their applicability to stainless steel CHS columns after exposure to fire, based on the experimental and numerical data.

2. Experimental study

2.1 General

Two circular hollow sections CHS 73×3 and CHS 89×3, cold-rolled and seam-welded from grade EN 1.4301 austenitic stainless steel sheets, were adopted in the testing programme. The cross-section designation system consists of the letters 'CHS' (indicating a circular hollow section) and the nominal section size in millimetres (outer cross-section diameter D × wall thickness t). Both of the two cross-sections at ambient temperature are categorised as Class 1 according to the slenderness limits specific in EN 1993-1-4 [25]. Two nominal member lengths respectively equal to six and nine times the nominal outer cross-section diameter were employed for the CHS 73×3 column specimens, leading to two specimen series D73-L6 and D73-L9; the designation system of the specimen series starts with a letter 'D' (representing diameter) and the nominal outer cross-section diameter in millimetre (i.e. 73), followed by a letter 'L' (signifying length), and ends with a number '6' or '9' (i.e. the ratio of the nominal member length to the nominal outer cross-section diameter), while the nominal lengths of the CHS 89×3 column specimens were all equal to six times the nominal outer cross-section diameter, with the resulting specimen series denoted as D89-L6. Each of the three specimen series includes five geometrically identical column specimens, with one unheated and the other four heated to various levels of elevated temperatures (with the target values of 300 °C, 600 °C, 800 °C and 1000 °C, respectively). The identifier of each specimen contains the specimen series, a letter 'T' (representing temperature) and the target elevated temperature, e.g., D89-L6-T800 represents a CHS 89×3 column specimen with the nominal member length equal to six times the nominal outer cross-section diameter and the target heating temperature of 800 °C. Table 1 summarises the target heating temperature T_n and the measured geometric dimensions of each column specimen. In the following Section 2.2, the detailed heating, soaking and cooling processes were described, while the material tensile coupons tests, initial geometric imperfection measurements and pin-ended column tests were respectively reported in Sections 2.3–2.5.

2.2 Heating, soaking and cooling processes

A Nabertherm forced convection furnace was used to heat the specimens. The chamber of the furnace, as shown in Fig. 1, contains a series of embedded heating elements distributed uniformly over the four sides, and is also equipped with a fan and air baffles to allow for air circulation during heating, thus ensuring a high degree of temperature uniformity within the chamber. The columns specimens, together with the coupon specimens cut from the stainless steel CHS tubes, were placed on the bottom air baffle and just in front of the fan (where the optimum air circulation during heating was achieved), and then heated from the ambient temperature to each pre-specified level of elevated temperature at a rate of 10 ºC/min, which is similar to the temperature increase rate of protected steelwork in fire. Upon attainment of the target temperature, it was maintained for half an hour (i.e. the soaking time of 30 mins), to ensure that the surface temperatures of the specimens were stable and uniform. When the soaking period was completed, the furnace was switched off, and the column and coupon specimens were naturally cooled down to the ambient temperature. During the heating, soaking and cooling processes, the actual surface temperatures of each group of column and coupon specimens (i.e. the specimens heated together to the same target elevated temperature) were measured through two thermocouples attached to the outer and inner surfaces of a representative column specimen, as depicted in Fig. 1. The temperatures measured at the inner and outer surfaces of each representative column specimen were almost the same during the whole heating, soaking and cooling processes; the temperature−time curves, recorded by the two thermocouples, for a typical group of specimens exposed to a target level of elevated temperature equal to 600 °C are depicted in Fig. 2. The measured maximum surface temperature *T* for each group of specimens, taken as the average reading from the thermocouples during the soaking period, is presented in Table 1. Grade EN 1.4301 austenitic stainless steel displayed obvious changes in surface colour after exposure to elevated temperatures [24]. As exhibited in Fig. 3, the surface colours of grade EN 1.4301 austenitic stainless steel turned into bright yellow, dark red, dark grey and black after exposure to elevated temperatures of 300 °C, 581 °C, 804 °C and 1007 °C.

2.3 Material tensile coupon tests

Upon completion of the heating, soaking and cooling processes, tensile coupon tests were conducted by using a 50 kN servo-hydraulic tensile testing machine. A displacement-controlled loading scheme was used to drive the actuator of the testing machine; the loading rate was initially set to be equal to 0.05 mm/min up to the material nominal 0.2% proof stress (yield stress) at ambient temperature, after which a faster loading rate equal to 0.8 mm/min was employed for the post-yield stage, as recommended by Huang and Young [28]. The tensile coupon test setup is displayed in Fig. 4, where an extensometer is mounted onto the coupon to record the elongation between the 50 mm gauge length, and a pair of strain gauges are attached to the mid-height of the coupon to capture the tensile strains. The measured (post-fire and ambient temperature) stress−strain curves of the tensile coupons, extracted from CHS 73×3 and CHS 89×3, are displayed in Figs 5(a) and 5(b), respectively, while the key measured material properties are listed in Table 2, including the Young's modulus *E*, the 0.2% proof stress $\sigma_{0.2}$, the ultimate strength σ_u, the strain at the ultimate strength ε_u, and the coefficients adopted in the component Ramberg–Osgood material model n and m [24, 29-34]. It was generally found that the material Young's modulus and ultimate strength almost remain unchanged as the heating temperature increases, while the material 0.2% proof stress does not exhibit visible reductions for heating temperatures up to 600 °C, but experiences relatively rapid decreases at higher heating temperatures. A more detailed discussion on the material properties and stress–strain responses of grade EN 1.4301 austenitic stainless steel after exposure to elevated temperatures was presented by the authors in He et al. [24].

2.4 Initial geometric imperfection measurements

The flexural buckling behaviour and strengths of column members are sensitive to their initial global geometric imperfections. Thus, the initial global geometric imperfection of each stainless steel CHS column specimen was carefully measured prior to the pin-ended column tests. The experimental setup for initial global geometric imperfection measurements is shown in Fig. 6, where the column specimen is mounted on the work bench of a CNC router, and a LVDT is moved along the uppermost edge line of the specimen, with the readings respectively recorded near the two ends and at mid-height. The initial mid-height global geometric imperfection magnitude of the column specimen in the radial direction was given as the deviation from a linear reference line (i.e. a linear line connecting the data points at the two ends) to the measured data point at mid-height. The specimen was then rotated at an interval of 60 degrees, with the measurement procedures repeated, to derive the initial global geometric imperfection magnitudes in another five radial directions – see Fig. 6. The value of the initial global geometric imperfection of each column specimen ω_g was defined as the maximum magnitude measured in all the six radial directions, as reported in Table 1.

2.4 Pin-ended column tests

Compression tests of pin-ended stainless steel CHS columns after exposure to fire were carried out, aimed at examining their post-fire flexural buckling behaviour and strengths, while comparative experiments were also conducted on the unheated reference column specimens. All the column specimens were loaded in an Instron 5000 kN servo-hydraulic testing machine at a constant rate equal to 0.2 mm/min. Each end of the testing machine is equipped with a knife-edge device, offering pin-ended boundary condition to the specimens. The knife-edge device, as depicted in Fig. 7, consists of a pit plate with a semi-circular groove and a wedge plate containing a knife-edge wedge. Prior to testing, each column specimen was positioned between the top and bottom knife-edge devices, and oriented such that the radial direction leading to the maximum initial global geometric imperfection magnitude was perpendicular to the knife-edges. It is worth noting that the distance from the rotation centre of the knife-edge device to the end of the column specimen is equal to 55 mm; thus the effective member length of each column specimen is given as L_e=L+110 mm, as listed in Table 1.

The column test rig is depicted in Fig. 7, including two LVDTs, positioned to the mid-height of the specimen, to measure the lateral deflections along the buckling direction, and a pair of strain gauges, sticked to the extreme fibres of the mid-height cross-section, to record the strains at these two positions along the longitudinal direction. The LVDT readings were adopted, together with the strain gauge values, to calculate the actual initial loading eccentricity about the buckling axis of each column specimen according to Eq. (1) [22, 35-38], where e_0 is the calculated initial loading eccentricity, N is the applied compression load, ε_{max}-ε_{min} is the difference of the longitudinal strains measured from the two strain gauges, Δ is the mid-height lateral deflection and I is the second moment of area of the circular hollow section; note that

Eq. (1) was derived based on an assumption that the structural behaviour was close to linear elastic, and it was thus recommended [22, 37, 38] that no more than 15% of the expected failure load be used in the calculation of e_0. If the calculated initial loading eccentricity, combined with the initial global geometric imperfection magnitude (i.e. ω_g+e_0), exceeded $L_e/1000$ [1, 21, 35], the position of the column specimen was carefully re-adjusted until the achievement of $(\omega_g+e_0)<L_e/1000$.

$$e_0 = \frac{EI(\varepsilon_{\max}-\varepsilon_{\min})}{DN} - \Delta - \omega_g \tag{1}$$

The experimental load–mid-height lateral deflection curves for the three series of stainless steel CHS column specimens are shown in Fig. 8. Table 3 summarised the key experimental results for the unheated and post-fire stainless steel CHS column specimens, including the combined initial global geometric imperfection magnitude and loading eccentricity (ω_g+e_0), the failure load N_u and the mid-height lateral deflection at the failure load δ_u. In terms of the deformed failure modes, flexural buckling was generally observed for all the three specimen series; Fig. 9 depicts the experimental failure modes for a typical specimen series D73-L9, including one unheated column specimen D73-L9-T30 and four post-fire column specimens D73-L9-T300, D73-L9-T600, D73-L9-T800 and D73-L9-T1000.

3. Numerical modelling

3.1 General

In parallel with the experimental study, a numerical modelling programme was carried out by means of the finite element analysis package ABAQUS [39], and reported in this section. Finite element (FE) models were firstly developed and validated against the experimental results.

Parametric studies were then conducted using the validated FE models, to derive further numerical data over an extended range of cross-section sizes and member lengths.

3.2 Development of FE models

Each stainless steel CHS column FE model was developed based on the measured cross-section geometric sizes and effective member lengths, as reported in Table 1. The shell element S4R [39] has been shown to be accurate and effective in previous numerical modelling of various types of stainless steel CHS structural components (e.g., columns [21, 40-42], beams [43] and beam-columns [13, 22, 23]), and was also adopted herein. The size of the employed S4R element was selected to be equal to $0.1D$, based on a prior mesh sensitivity study [24]; this element size was shown to be capable of offering both satisfactory computational efficiency and accuracy. With regard to the material modelling, the ambient temperature and post-fire material stress–strain curves measured from the tensile coupon tests were firstly converted into the true stress–true plastic strain curves, and afterwards assigned to the respective FE modes for stainless steel CHS columns at ambient temperature and after exposure to fire. For the ease of defining the boundary condition, all the nodes of each end section of the stainless steel CHS column FE model were coupled to a concentric reference point. The top reference point (at the loaded end) were restrained except for rotation about the buckling axis as well as longitudinal translation, whilst the bottom reference point was only allowed to rotate about the buckling axis, to replicate the same pin-ended boundary condition as that adopted in the tests. The initial local and global geometric imperfections were included into each stainless steel CHS column FE model in the form of the lowest elastic local and global buckling mode shapes [21, 22], as derived from the eigenvalue buckling analysis [39]. Two levels of initial local imperfection magnitudes, namely 1/100 and 1/10 of the wall thickness [13, 22], and three levels of initial global imperfection values, including the measured total global imperfection value (ω_g+e_0) and 1/1000 and 1/1500 of the member effective length, were adopted to factor the corresponding initial geometric imperfection patterns for each stainless steel CHS column FE model, resulting in a total of six combinations of initial local and global geometric imperfection magnitudes to be examined. The six initial local and global geometric imperfection magnitude combinations were employed to assess the influence of the initial geometric imperfection magnitudes on the ambient temperature and post-fire mechanical behaviour of stainless steel CHS columns and seek the most appropriate initial geometric imperfection magnitude combination to be employed in the parametric studies.

3.3 Validation of FE models

Upon development of the stainless steel CHS column FE models, Riks analysis was performed to obtain the numerical failure loads, load–mid-height lateral deflection curves and failure modes, which were afterwards compared against their experimental counterparts, enabling the accuracy of the developed FE models to be assessed. Table 4 lists the test to numerical failure load ratios for the six combinations of initial local and global geometric imperfection magnitudes. It is evident that the experimental failure loads of the stainless steel CHS column specimens at ambient temperature and after exposure to fire were generally well captured for all the six examined initial geometric imperfection magnitude combinations. It is also worth noting that although the overall accuracy is deemed to be satisfied, there still exist discrepancies between the experimental and numerical failure loads for some specimens, with the main potential reason being that the actual initial geometric imperfections of the specimens and the idealised initial geometric imperfections (with elastic buckling mode shapes) of the FE modes are different. Moreover, the influence of the initial local geometric imperfection magnitudes on the numerically predicted failure loads was much less significant than that of the initial global geometric imperfection magnitudes for the stainless steel CHS column specimens with non-slender cross-sections. The best agreement between the test and numerical failure loads was obtained when the measured total global imperfection magnitude (ω_g+e_0) and the initial local imperfection magnitude of $t/100$ were adopted, while the combination, with the initial global imperfection magnitude of $L_e/1000$ and initial local imperfection magnitude of $t/100$ also led to accurate numerical failure loads. The numerical load–mid-height lateral deflection curves for a typical specimen series D73-L6 are displayed in Fig. 10, together with their experimental counterparts, where the initial stiffnesses, general shapes and post-peak responses of the test load–deformation histories are found to be well replicated. Comparisons between the experimental and numerical failure modes for the typical specimen series D73-L9 are illustrated in Fig. 9, also indicating good agreement. Overall, the developed FE models are capable of accurately simulating the experimental flexural buckling responses of stainless steel CHS columns at ambient temperature and after exposure to fire, and thus deemed to be validated.

3.4 Parametric studies

Having been validated in Section 3.3, the developed column FE models were subsequently used to conduct parametric studies, aimed at expanding the test data pool on stainless steel CHS columns after exposure to fire over an extended range of cross-section sizes and member lengths. Specifically, the outer cross-section diameter D was kept at 100 mm, with the wall thicknesses t varied between 0.86 mm and 4.65 mm; this leads to the $D/t\varepsilon^2$ ratios at ambient temperature ranging from 30 to 90, and covers all the three EC3 non-slender classes (i.e. Class 1, 2 and 3) of circular hollow sections. The effective member lengths of the column FE models were set to be varied between 500 mm (i.e. five times the outer cross-section diameter) and 5500 mm (i.e. fifty-five times the outer cross-section diameter). The modelling procedures and techniques relevant to the development of stainless steel CHS column FE models, as presented in Section 3.2, were also employed in the present parametric studies, but with some supplementary information highlighted herein: (i) the measured material stress–strain curves of CHS 73×3 at ambient temperature and after exposure to four levels of elevated temperatures were used, and (ii) the initial local and global geometric imperfection magnitudes were respectively set to be equal to $t/100$ and $L_e/1000$. In sum, a total of 385 numerical data on stainless steel CHS columns at ambient temperature and after exposed to fire were generated in the parametric studies.

4. Evaluation of existing design standards

4.1 General

Due to the absence of established standards for the design of stainless steel structures after exposure to fire, the relevant design rules for stainless steel CHS columns at ambient temperature, as specified in the European code EN 1993-1-4 [25], American specification SEI/ASCE-8 [26] and Australian/New Zealand standard AS/NZS 4673 [27], were assessed herein for their applicability to stainless steel CHS columns after exposure to fire. In each of the following sub-sections, the codified design rules and formulations for stainless steel CHS columns at ambient temperature were firstly described. The unfactored flexural buckling strengths of the examined stainless steel CHS columns after exposure to fire were then calculated, based on the ambient temperature design formulations but with the post-fire material properties. Quantitative evaluation of the applicability of each design standard was conducted by comparing the unfactored post-fire flexural buckling strengths N_u against the test and numerical failure loads $N_{u,pred}$, with the mean ratios of $N_u/N_{u,pred}$ and corresponding coefficients of variation (COVs) summarised in Table 5.

4.2 European code EN 1993-1-4 (EC3)

The existing European code EN 1993-1-4 [25] adopts buckling curves for the design of stainless steel column members prone to global buckling (e.g., torsional, flexural and flexural-torsional buckling) at ambient temperature. With regards to stainless steel CHS columns failing by flexural buckling, the EC3 design strengths are given by Eq. (2),

$$N_{u,EC3} = \chi A \sigma_{0.2} \tag{2}$$

where A is the cross-section area, respectively equal to the gross section area A_g and effective section area A_{eff} for Class 1, 2 and 3 (non-slender) and Class 4 (slender) circular hollow sections, and χ is the reduction factor, as determined from the EC3 design buckling curve for stainless steel CHS columns and given by Eq. (3),

$$\chi = \frac{1}{\phi + \sqrt{\phi^2 - \bar{\lambda}^2}} \leq 1 \tag{3}$$

where $\bar{\lambda}$ is the member non-dimensional slenderness and determined by Eq. (4), while ϕ is a buckling coefficient and calculated from Eq. (5), in which $\bar{\lambda}_0$ and α are respectively the limiting slenderness and imperfection factor; for stainless steel CHS columns, $\bar{\lambda}_0 = 0.4$ and α=0.49.

$$\bar{\lambda} = \sqrt{\frac{A\sigma_{0.2} L_e^2}{\pi^2 EI}} \tag{4}$$

$$\phi = 0.5[1+\alpha(\bar{\lambda}-\bar{\lambda}_0)+\bar{\lambda}^2] \quad (5)$$

The EC3 design flexural buckling strengths of stainless steel CHS columns after exposure to fire were calculated herein using Eqs (2)–(5), but with the ambient temperature material properties replaced by the corresponding post-fire material properties, and then compared against the experimental and numerical failure loads. The mean ratios of $N_u/N_{u,EC3}$ and the corresponding COVs for stainless steel CHS columns at ambient temperature and after exposure to various levels of elevated temperatures are reported in Table 5. The quantitative evaluation results revealed that the EC3 design flexural buckling curve generally yields inaccurate (unsafe and scattered) predictions of strengths for stainless steel CHS columns at ambient temperature and after exposed to fire. Fig. 11 depicts the normalised failure loads of stainless steel CHS columns at ambient temperature and after exposure to fire (by the cross-section yield loads $A\sigma_{0.2}$) plotted against the member non-dimensional slendernesses, together with the EC3 design flexural buckling curve; note that the cross-section yield loads and member non-dimensional slendernesses for stainless steel CHS columns after exposure to fire were calculated, based on the corresponding post-fire material properties. It is also evident in Fig. 11 that (i) the normalised data points of stainless steel CHS columns at ambient temperature and after exposure to fire exhibit rather small differences and (ii) the EC3 design flexural buckling curve yields unsafe strength predictions for stainless steel CHS columns at ambient temperature and after exposure to fire. It is worth noting that the EC3 design flexural buckling curve for stainless steel cold-formed hollow section columns at ambient temperature was calibrated based mainly on the square hollow section (SHS) and rectangular hollow section (RHS) column buckling test results, due to the lack of CHS column test data at the time when the standard was produced. Cold-formed SHS and RHS benefit from material strength enhancements at the corner regions, and hence the EC3 design flexural buckling curve calibrated based on the SHS and RHS column test data results in unsafe flexural buckling strength predictions when applied to CHS columns.

4.2 American specification SEI/ASCE-8 (ASCE)

The American specification SEI/ASCE-8 [26] specifies that the design axial strength of stainless steel concentrically loaded compression member at ambient temperature is calculated as the product of the design failure stress F_n and the effective cross-section area A_e determined at the design failure stress, as given by Eq. (6). For doubly-symmetric tubular section columns which are prone to flexural buckling but not susceptible to torsional and flexural-torsional buckling, the design failure stress is equal to the corresponding design flexural buckling stress, as derived from Eq. (7) using the tangent modulus method, in which E_T is the tangent modulus of the material stress–strain curve at the design flexural buckling stress point; note that cumbersome iterations are generally required in the determination of E_T and F_n. The effective cross-section area A_e is given by Eq. (8), where K_c is the reduction factor and determined from Eq. (9), in which C is the material proportional limit to 0.2% proof stress ratio and λ_c=3.048C.

$$N_{u,ASCE} = F_n A_e \tag{6}$$

$$F_n = \frac{\pi^2 E_T}{(kL/r)^2} \le \sigma_{0.2} \tag{7}$$

$$A_e = [1-(1-(\frac{E_T}{E})^2)(1-K_c)]A \tag{8}$$

$$K_c = \frac{(1-C)(E/\sigma_{0.2})}{(8.93-\lambda_c)(D/t)} + \frac{5.882C}{8.93-\lambda_c} \le 1 \tag{9}$$

The ASCE design axial strengths of stainless steel CHS columns after exposure to fire were calculated, based on Eqs (6)–(9) and the post-fire material properties, and compared with the corresponding test and numerical failure loads in Fig. 12, together with the ambient temperature data points. It was found that the SEI/ASCE-8 design flexural buckling strengths are generally unsafe for stainless steel CHS columns at ambient temperature and after exposure to fire; this can also be seen from the quantitative evaluation results given in Table 5. Note that the design stress in the tangent modulus method of SEI/ASCE-8 [26] is actually the Euler buckling stress derived with the use of tangent modulus. The design stress does not consider any detrimental effect from the initial global geometric imperfection, and is thus shown to overestimate the actual failure stress of stainless steel columns. Moreover, SEI/ASCE-8 [26] was shown to yield even more over-predicted though marginally more consistent flexural buckling strengths than EN 1993-1-4 [25].

4.3 Australian/New Zealand standard AS/NZS 4673 (AS/NZS)

Regarding the calculation of design axial strengths of stainless steel concentrically loaded compression members at ambient temperature, the Australian/New Zealand standard AS/NZS 4673 [27] uses the same approach as that adopted in SEI/ASCE-8 [26], but also provides an alternative explicit approach [44]. Similarly to the EC3 design buckling curves, the AS/NZS explicit approach was also developed in accordance with the Perry-Robertson buckling formula. The design flexural buckling stress F_a is calculated from Eq. (10), in which $\bar{\lambda}$ is the member non-dimensional slenderness and can be determined from Eq. (4), and ϕ_a is the AS/NZS buckling coefficient and defined by Eq. (11), where α, β, λ_0 and λ_1 are the parameters depending on the stainless steel grades; note that the values of α, β, λ_0 and λ_1 are respectively taken as 1.59, 0.28, 0.55 and 0.2 for the studied grade EN 1.4301 (i.e. Type 304) austenitic stainless steel. The AS/NZS design column flexural buckling strength is then calculated from Eq. (12) as the product of the design flexural buckling stress F_a and the effective cross-section area determined at the design flexural buckling stress A_e; note that A_e is also calculated from Eq. (8), but with a different reduction factor given by Eq. (13).

$$F_a = \frac{\sigma_{0.2}}{\phi_a + \sqrt{\phi_a^2 - \bar{\lambda}^2}} \leq \sigma_{0.2} \tag{10}$$

$$\phi_a = 0.5\left\{1 + \alpha[(\bar{\lambda} - \lambda_1)^{\beta} - \lambda_0] + \bar{\lambda}^2\right\} \tag{11}$$

$$N_{u,AS/NZS} = F_a A_e \tag{12}$$

$$K_c = \frac{(1-C)(E/\sigma_{0.2})}{(3.226-\lambda_c)(D/t)} + \frac{0.178C}{3.226-\lambda_c} \leq 1 \tag{13}$$

Evaluation of the applicability of the AS/NZS explicit approach to the design of stainless steel CHS columns after exposure to fire was carried out herein through comparing the post-fire flexural buckling strengths (calculated using Eqs (10)–(13) and the post-fire material properties) with the experimental and numerical failure loads. Fig. 13 presents the $N_u/N_{u,AS/NZS}$ ratios plotted against the member non-dimensional slendernesses for both the ambient temperature and post-fire data points. The design flexural buckling curve defined by the AS/NZS explicit approach, as also depicted in Fig. 13, was shown to be capable of capturing the test and numerical data points across the full range of member non-dimensional slenderness $\bar{\lambda}$ and resulting in safe, accurate and consistent flexural buckling strength predictions for stainless steel CHS columns after exposure to fire as well as at ambient temperature. The mean test (or numerical) to AS/NZS predicted failure load ratio $N_u/N_{u,AS/NZS}$ and the corresponding COV, as listed in Table 5, are equal to 1.119 and 0.103, respectively. Both the graphical and quantitative evaluation results revealed that the AS/NZS 4673 explicit design approach for stainless steel CHS columns at ambient temperature can be safely applied to their counterparts after exposure to fire, with a high degree of design accuracy and consistency. It is worth noting that the AS/NZS explicit approach was derived and calibrated based on a comprehensive set of finite element data [44], including those for CHS columns, and thus found to yield more accurate and consistent flexural buckling strength predictions in comparison with the EC3 design buckling curve and ASCE tangent modulus method.

5. Conclusions

A thorough experimental and numerical investigation has been performed to examine the flexural buckling behaviour and residual strengths of stainless steel CHS columns after exposure to fire. The experimental study was performed on 12 austenitic stainless steel CHS column specimens after exposure to four levels of elevated temperatures and 3 unheated reference column specimens, and included material tensile coupon tests, initial geometric imperfection measurements and pin-ended column tests. In parallel with the experimental study, a numerical investigation was conducted. FE models were initially developed and validated against the experimental results, and then adopted to perform parametric studies, aimed at deriving further numerical data over an extended range of member lengths and cross-section sizes. Given that there have been no codified post-fire design rules for stainless steel CHS columns, the corresponding ambient temperature design rules, as specified in the current EN 1993-1-4 [25], SEI/ASCE-8 [26] and AS/NZS 4673 [27], were assessed for their applicability to stainless steel CHS columns after exposure to fire, based on the experimental and numerical data. It was found that (i) the normalised data points of stainless steel CHS columns at ambient temperature and after exposure to fire (i.e. the failure loads normalised by the cross-section yield loads) exhibit rather small differences and (ii) the design buckling curve, as employed in EN 1993-1-4 [25], and the tangent modulus method, as adopted in SEI/ASCE-8 [26], yield generally unsafe and rather scattered predictions of flexural buckling strengths for stainless steel CHS columns after exposure to fire, and (iii) the explicit approach, as used in AS/NZS

4673 [27], was shown to lead to a high level of accuracy and consistency in the design of stainless steel CHS columns after exposure to fire, with safe, accurate and consistent post-fire flexural buckling strength predictions.

References

[1] Rasmussen KJR, Hancock GJ. Design of Cold‐Formed Stainless Steel Tubular Members. I: Columns. Journal of Structural Engineering. 1993;119:2349-67.

[2] Burgan BA, Baddoo NR, Gilsenan KA. Structural design of stainless steel members comparison between Eurocode 3, Part 1.4 and test results. Journal of Constructional Steel Research. 2000;54:51-73.

[3] Rasmussen KJR. Recent research on stainless steel tubular structures. Journal of Constructional Steel Research. 2000;54:75-88.

[4] Young B, Hartono W. Compression tests of stainless steel tubular members. J Struct Eng-Asce. 2002;128:754-61.

[5] Gardner L, Nethercot DA. Experiments on stainless steel hollow sections - Part 1: Material and cross-sectional behaviour. Journal of Constructional Steel Research. 2004;60:1291-318.

[6] Bardi FC, Kyriakides S. Plastic buckling of circular tubes under axial compression - part I: Experiments. Int J Mech Sci. 2006;48:830-41.

[7] Paquette JA, Kyriakides S. Plastic buckling of tubes under axial compression and internal pressure. Int J Mech Sci. 2006;48:855-67.

[8] Lam D, Gardner L. Structural design of stainless steel concrete filled columns. Journal of Constructional Steel Research. 2008;64:1275-82.

[9] Uy B, Tao Z, Han LH. Behaviour of short and slender concrete-filled stainless steel tubular columns. Journal Of Constructional Steel Research. 2011;67:360-78.

[10] Rasmussen KJR, Hancock GJ. Design of Cold-Formed Stainless-Steel Tubular Members .2. Beams. J Struct Eng-Asce. 1993;119:2368-86.

[11] Kiymaz G. Strength and stability criteria for thin-walled stainless steel circular hollow section members under bending. Thin-Walled Structures. 2005;43:1534-49.

[12] A. Talja, Test Report on Welded I and CHS Beams, Columns and Beam-Columns (Report to ECSC), VTT Building Technology, Finland, 1997.

[13] Zhao O, Gardner L, Young B. Structural performance of stainless steel circular hollow sections under combined axial load and bending – Part 1: Experiments and numerical modelling. Thin-Walled Structures. 2016;101:231-9.

[14] Zhao O, Gardner L, Young B. Structural performance of stainless steel circular hollow sections under combined axial load and bending – Part 2: Parametric studies and design. Thin-Walled Structures. 2016;101:240-8.

[15] Buchanan C, Gardner L, Liew A. The continuous strength method for the design of circular hollow sections. Journal of Constructional Steel Research. 2016;118:207-16.

[16] Afshan S, Gardner L. The continuous strength method for structural stainless steel design. Thin-Walled Structures. 2013;68:42-9.

[17] Zhao O, Afshan S, Gardner L. Structural response and continuous strength method design of slender stainless steel cross-sections. Engineering Structures. 2017;140:14-25.

[18] Ashraf M, Gardner L, Nethercot DA. Compression strength of stainless steel cross-sections. Journal of Constructional Steel Research. 2006;62:105-15.

[19] Ashraf M, Gardner L, Nethercot DA. Structural Stainless Steel Design: Resistance Based on Deformation Capacity. Journal of Structural Engineering. 2008;134:402-11.

[20] Gardner L. The continuous strength method for hot-rolled steel and steel-concrete composite design. Proceedings of the Institution of Civil Engineers - Structures and Buildings. 2008;161:127-33.

[21] Buchanan C, Real E, Gardner L. Testing, simulation and design of cold-formed stainless steel CHS columns. Thin-Walled Structures. 2018;130:297-312.

[22] Zhao O, Gardner L, Young B. Testing and numerical modelling of austenitic stainless steel CHS beam–columns. Engineering Structures. 2016;111:263-74.

[23] Buchanan C, Zhao O, Real E, Gardner L. Cold-formed stainless steel CHS beam-columns – testing, simulation and design. Engineering Structures. (in press).

[24] He A, Liang Y, Zhao O. Experimental and numerical studies of austenitic stainless steel CHS stub columns after exposed to elevated temperatures. Journal of Constructional Steel Research. 2019;154:293-305.

[25] EN 1993-1-4:2006+A1:2015. Eurocode 3: design of steel structures – part 1. 4: general rules – supplementary rules for stainless steels, including amendment A1 (2015). Brussels: European Committee for Standardization (CEN); 2015.

[26] SEI/ASCE 8-02, Specification for the design of cold-formed stainless steel structural members, American Society of Civil Engineers (ASCE), Reston, 2002.

[27] AS/NZS 4673. Cold-formed stainless steel structures. Sydney: AS/NZS 4673:2001; 2001.

[28] Huang Y, Young B. The art of coupon tests. Journal of Constructional Steel Research, 2014;96:159-175.

[29] Ramberg W, Osgood WR. Description of stress–strain curves by three parameters. Technical note no. 902. Washington DC: National Advisory Committee for Aeronautics; 1943.

[30] Hill HN. Determination of stress–strain relations from offset yield strength values. Technical note no. 927. Washington DC: National Advisory Committee for Aeronautics; 1944.

[31] Mirambell E, Real E. On the calculation of deflections in structural stainless steel beams: an experimental and numerical investigation. Journal of Constructional Steel Research. 2000;54:109-33.

[32] Rasmussen KJR. Full-range stress–strain curves for stainless steel alloys. Journal of Constructional Steel Research. 2003;59:47-61.

[33] Arrayago I, Real E, Gardner L. Description of stress–strain curves for stainless steel alloys. Materials & Design. 2015;87:540-52.

[34] Tao Z, Wang X-Q, Hassan MK, Song T-Y, Xie L-A. Behaviour of three types of stainless steel after exposure to elevated temperatures. Journal of Constructional Steel Research. 2018.

[35] Gardner L, Bu Y, Theofanous M. Laser-welded stainless steel I-sections: Residual stress measurements and column buckling tests. Engineering Structures. 2016;127:536-48.

[36] Huang Y, Young B. Experimental investigation of cold-formed lean duplex stainless steel beam-columns. Thin-Walled Structures. 2014;76:105-17.

[37] Zhao O, Rossi B, Gardner L, Young B. Behaviour of structural stainless steel cross-sections under combined loading – Part I: Experimental study. Engineering Structures. 2015;89:236-46.

[38] Zhao O, Gardner L, Young B. Experimental Study of Ferritic Stainless Steel Tubular Beam-Column Members Subjected to Unequal End Moments. Journal of Structural Engineering. 2016;142.

[39] ABAQUS. ABAQUS/standard user’s manual volumes I–III and ABAQUS CAE manual. Version 6.12. Pawtucket (USA): Hibbitt, Karlsson & Sorensen, Inc; 2012.

[40] Mohammed A, Afshan S. Numerical modelling and fire design of stainless steel hollow section columns. Thin-Walled Structures. 2019;144.

[41] Huang Y, Young B. Design of cold-formed stainless steel circular hollow section columns using direct strength method. Engineering Structures. 2018;163:177-83.

[42] Chan T-M, Zhao X-L, Young B. Cross-section classification for cold-formed and built-up high strength carbon and stainless steel tubes under compression. Journal of Constructional Steel Research. 2015;106:289-95.

[43] Bock M, Gardner L, Real E. Material and local buckling response of ferritic stainless steel sections. Thin-Walled Structures. 2015;89:131-41.

[44] Rasmussen KJ, Rondal J. Strength curves for metal columns. Journal of Structural Engineering, 1997;123(6):721-728.

Table 1 Measured geometric properties of stainless steel CHS column specimens.

Specimen ID	D (mm)	t (mm)	L (mm)	L_e (mm)	T_n (°C)	T (°C)	ω_g (mm)
D73-L6-T30	72.72	2.79	438	548	30	30	0.04
D73-L6-T300	73.00	2.79	438	548	300	300	0.06
D73-L6-T600	72.97	2.80	438	548	600	581	0.03
D73-L6-T800	72.83	2.81	438	548	800	804	0.11
D73-L6-T1000	72.85	2.77	438	548	1000	1007	0.30
D73-L9-T30	72.73	2.79	658	768	30	30	0.09
D73-L9-T300	72.80	2.76	658	768	300	300	0.16
D73-L9-T600	72.70	2.78	658	768	600	581	0.12
D73-L9-T800	72.92	2.78	658	768	800	804	0.21
D73-L9-T1000	72.65	2.77	658	768	1000	1007	0.09
D89-L6-T30	89.87	2.78	534	644	30	30	0.14
D89-L6-T300	89.59	2.78	534	644	300	300	0.19
D89-L6-T600	89.11	2.76	534	644	600	581	0.13
D89-L6-T800	89.19	2.77	534	644	800	804	0.14
D89-L6-T1000	88.98	2.76	534	644	1000	1007	0.20

Table 2 Summary of key measured material properties from tensile coupon tests.

Cross-section	T (°C)	E (GPa)	$\sigma_{0.2}$ (MPa)	σ_u (MPa)	ε_u (%)	n	m
CHS 73×3	30	194	303	735	47	3.4	2.4
	300	205	290	730	46	3.6	2.4
	581	201	287	702	50	7.8	2.4
	804	204	262	708	49	4.9	2.3
	1007	205	177	700	51	5.7	1.9
CHS 89×3	30	206	292	727	55	4.0	2.4
	300	193	288	723	55	7.4	2.4
	581	208	323	718	61	3.9	2.6
	804	205	284	707	57	6.6	2.4
	1007	203	215	672	62	5.7	2.1

Table 3 Key experimental results of pin-ended stainless steel CHS columns at ambient temperature and after exposure to elevated temperatures.

Specimen ID	T (°C)	L (mm)	L_e (mm)	ω_g+e_0 (mm)	N_u (kN)	δ_u (mm)
D73-L6-T30	30	438	548	0.25	185.6	3.43
D73-L6-T300	300	438	548	0.29	198.1	2.04
D73-L6-T600	581	438	548	0.27	193.1	2.09
D73-L6-T800	804	438	548	0.35	178.5	2.26
D73-L6-T1000	1007	438	548	0.53	111.1	4.08
D73-L9-T30	30	658	768	0.19	186.5	2.25
D73-L9-T300	300	658	768	0.25	187.0	2.15
D73-L9-T600	581	658	768	0.21	189.8	2.07
D73-L9-T800	804	658	768	0.30	170.9	1.55
D73-L9-T1000	1007	658	768	0.18	123.3	2.68
D89-L6-T30	30	534	644	0.34	235.2	2.97
D89-L6-T300	300	534	644	0.39	241.3	2.22
D89-L6-T600	581	534	644	0.32	251.7	3.07
D89-L6-T800	804	534	644	0.34	232.1	2.93
D89-L6-T1000	1007	534	644	0.40	165.7	5.88

Table 4 Comparison of test failure loads with FE failure loads for various combinations of initial local and global geometric imperfection magnitudes.

Specimen	Test N_u /FE N_u					
	(ω_g+e_0)+t/100	L_e/1000+t/100	L_e/1500+t/100	(ω_g+e_0)+t/10	L_e/1000+t/10	L_e/1500+t/10
D73-L6-T30	0.915	0.929	0.921	0.916	0.930	0.922
D73-L6-T300	1.015	1.028	1.019	1.014	1.027	1.019
D73-L6-T600	1.040	1.056	1.046	1.039	1.055	1.045
D73-L6-T800	1.022	1.032	1.023	1.023	1.033	1.024
D73-L6-T1000	0.945	0.946	0.936	0.944	0.945	0.935
D73-L9-T30	0.992	1.036	1.019	0.993	1.036	1.019
D73-L9-T300	1.056	1.096	1.078	1.056	1.096	1.078
D73-L9-T600	1.143	1.178	1.164	1.143	1.178	1.166
D73-L9-T800	1.089	1.121	1.105	1.089	1.121	1.105
D73-L9-T1000	1.175	1.215	1.197	1.174	1.214	1.197
D89-L6-T30	0.967	0.979	0.971	0.967	0.980	0.972
D89-L6-T300	1.040	1.053	1.045	1.041	1.053	1.045
D89-L6-T600	0.966	0.978	0.970	0.966	0.980	0.971
D89-L6-T800	1.018	1.031	1.022	1.019	1.032	1.023
D89-L6-T1000	0.950	0.961	0.952	0.950	0.962	0.952
Mean	1.022	1.043	1.031	1.022	1.043	1.032
COV	0.071	0.079	0.077	0.071	0.079	0.077

Table 5 Comparisons of test and numerical failure loads with codified strength predictions.

Temperature	No. of test data	No. of numerical data	$N_u/N_{u,EC3}$		$N_u/N_{u,ASCE}$		$N_u/N_{u,AS/NZS}$	
			Mean	COV	Mean	COV	Mean	COV
T=30 °C	3	77	0.961	0.156	0.977	0.147	1.097	0.100
T=300 °C	3	77	0.954	0.162	0.978	0.148	1.091	0.097
T=581 °C	3	77	1.046	0.123	0.949	0.151	1.199	0.076
T=804 °C	3	77	0.977	0.150	0.962	0.153	1.121	0.082
T=1007 °C	3	77	0.934	0.204	0.970	0.180	1.084	0.122
Total	15	385	0.975	0.163	0.967	0.156	1.119	0.103

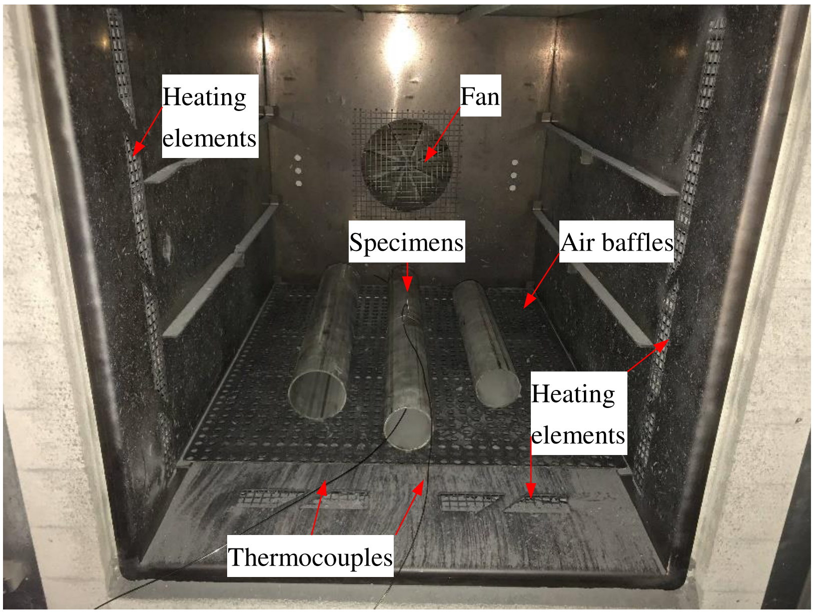

Fig. 1. Nabertherm forced convection furnace.

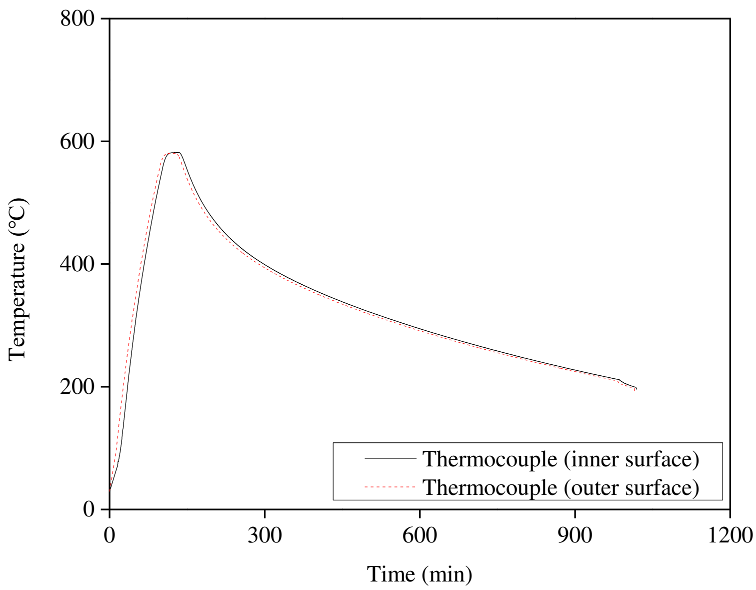

Fig. 2. Temperature–time curves for a typical group of specimens exposed to a target level of elevated temperature equal to 600 °C.

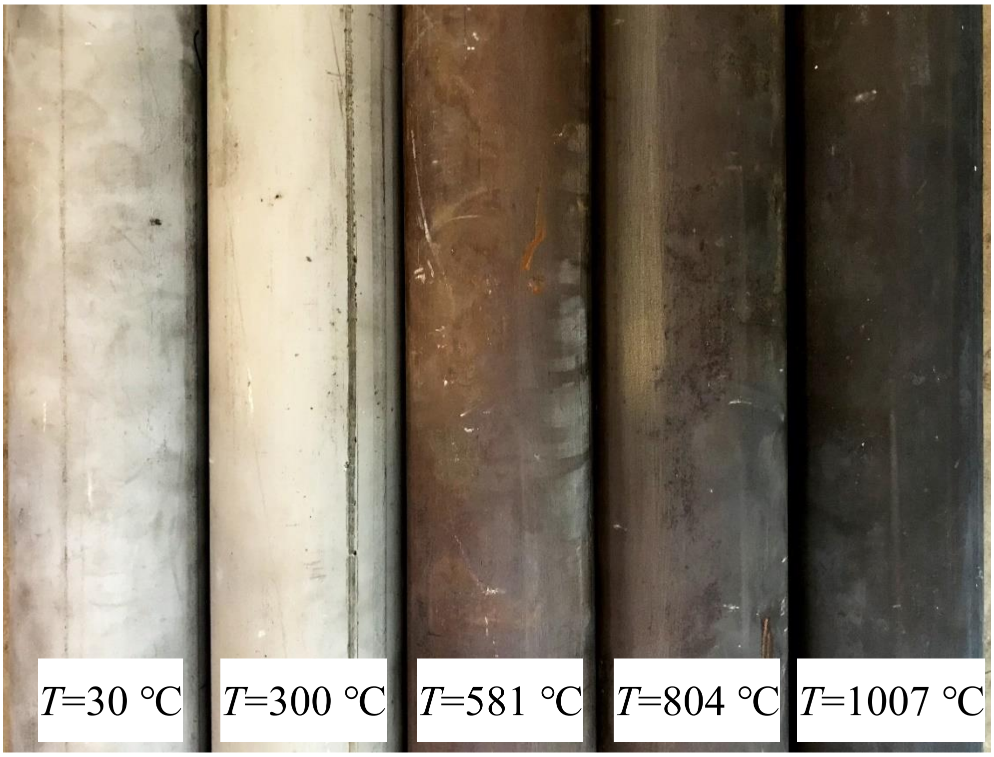

Fig. 3. Surface colours of austenitic stainless steel after exposure to various levels of elevated temperatures.

Fig. 4. Material tensile coupon test setup.

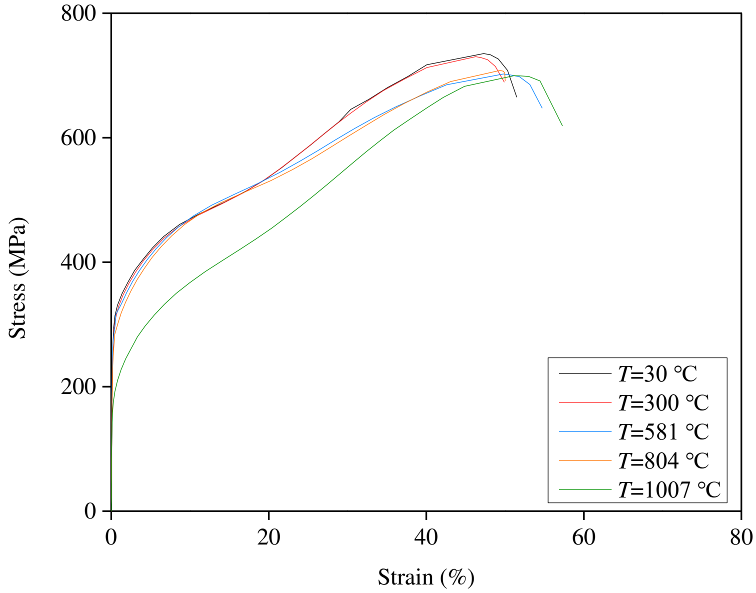

(a) CHS 73×3

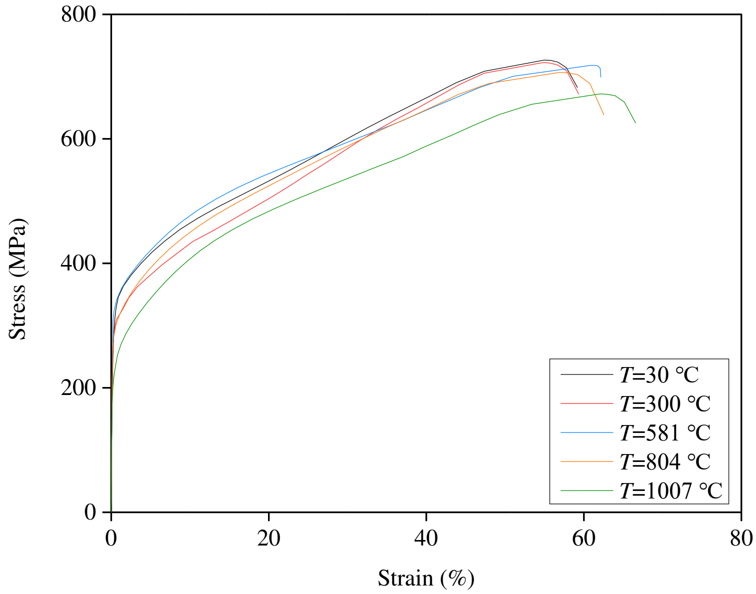

(b) CHS 89×3

Fig. 5. Stress–strain curves of austenitic stainless steel at ambient temperature and after exposure to different levels of elevated temperatures.

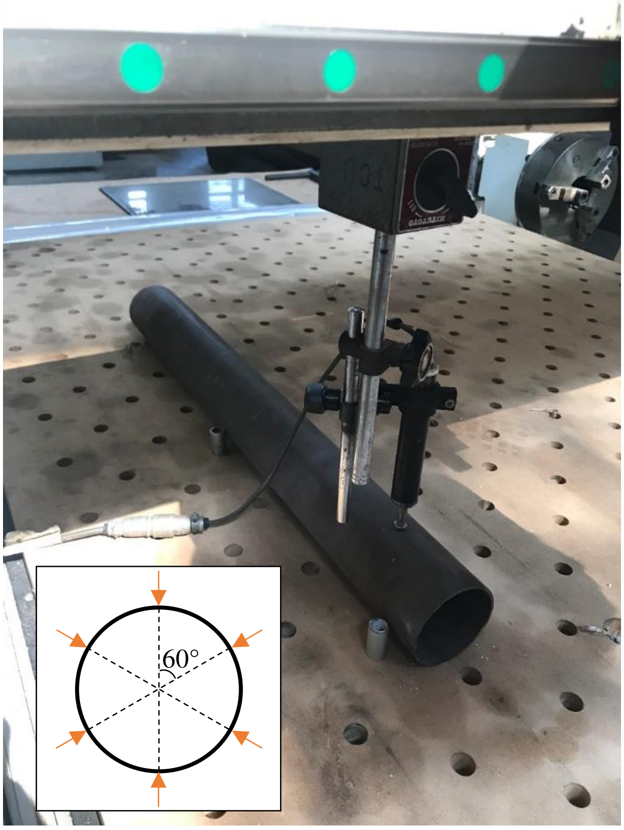

Fig. 6. Experimental setup for initial global geometric imperfection measurements.

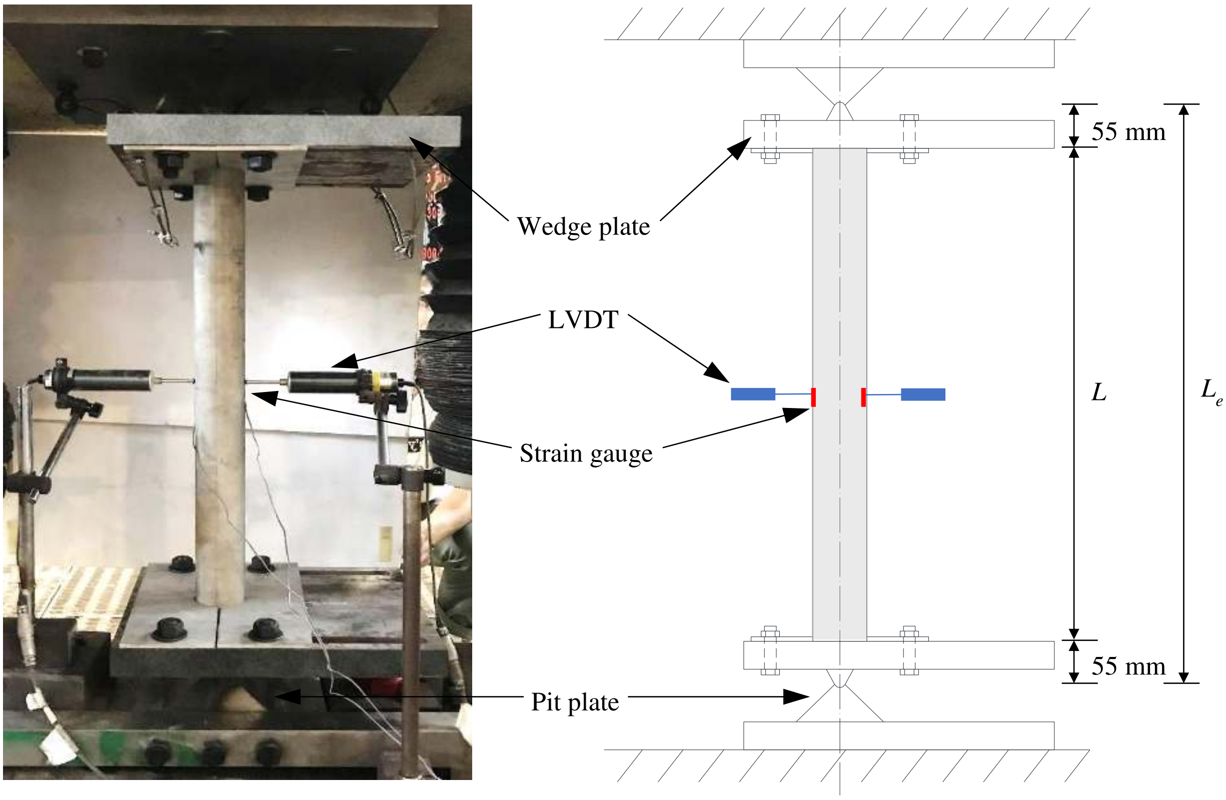

(a) Test setup (b) Schematic diagram of the test setup

Fig. 7. Column test configuration.

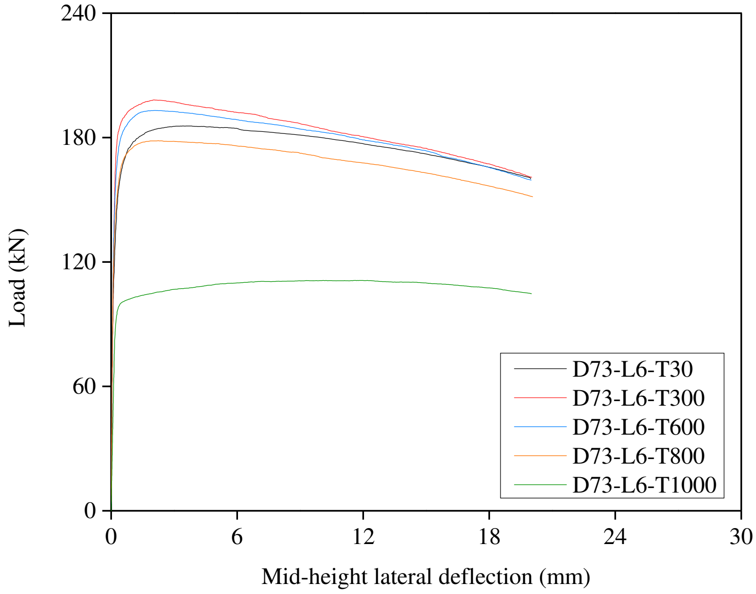

(a) Specimen series D73-L6

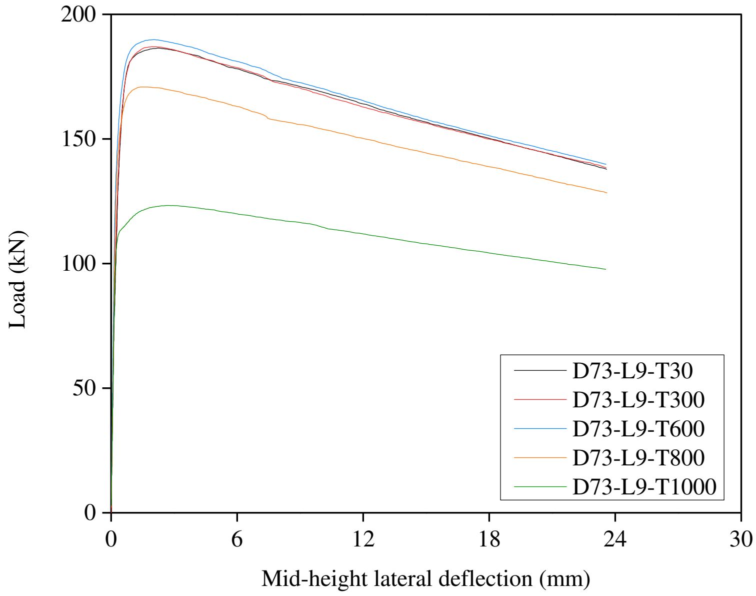

(b) Specimen series D73-L9

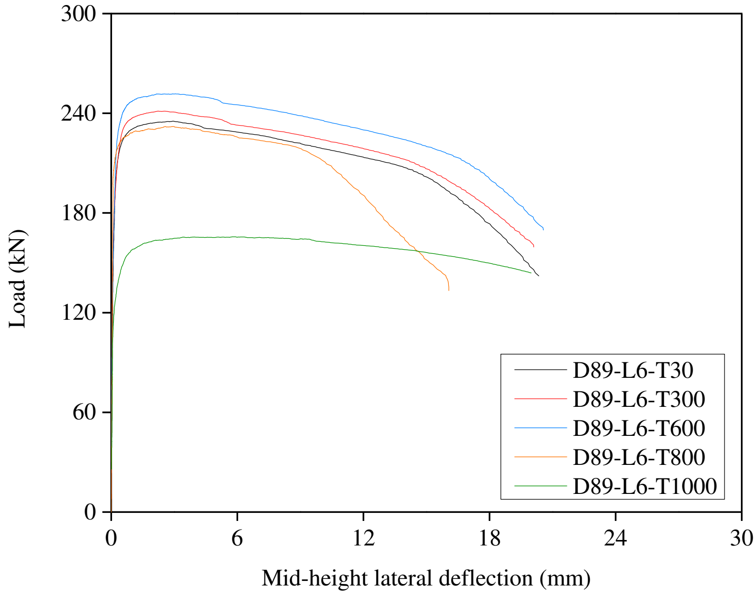

(c) Specimen series D89-L6

Fig. 8. Load–mid-height lateral deflection curves for pin-ended stainless steel CHS column specimens at room temperature and after exposure to elevated temperatures

(a) Experimental failure modes

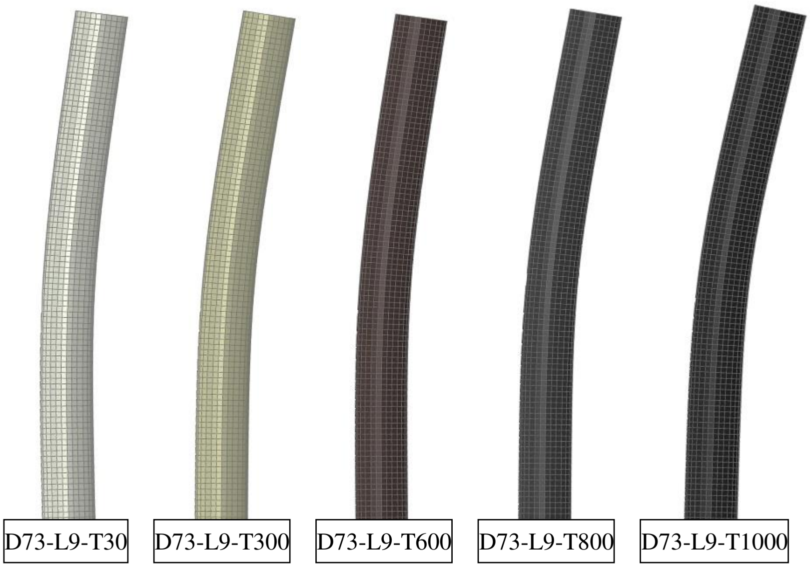

(b) Numerical failure modes

Fig. 9. Experimental and numerical failure modes for a typical specimen series D73-L9.

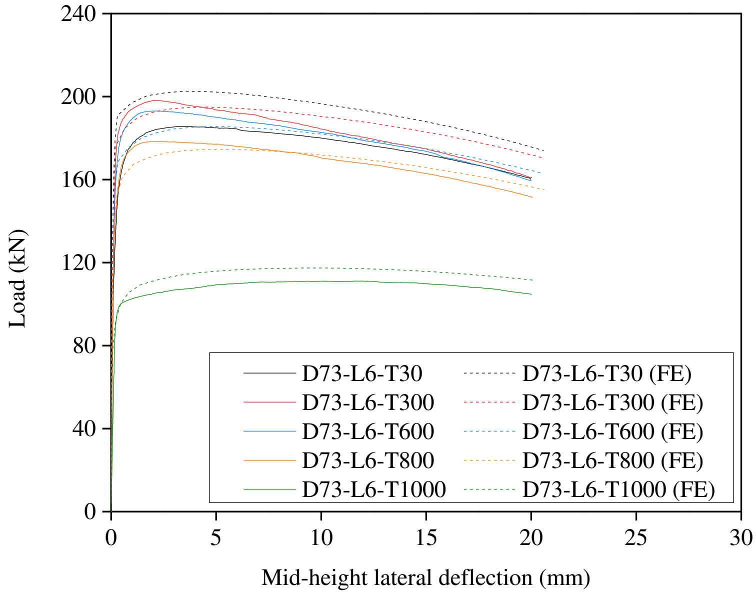

Fig. 10. Experimental and numerical load–mid-height lateral deflection curves for a typical specimen series D73-L6.

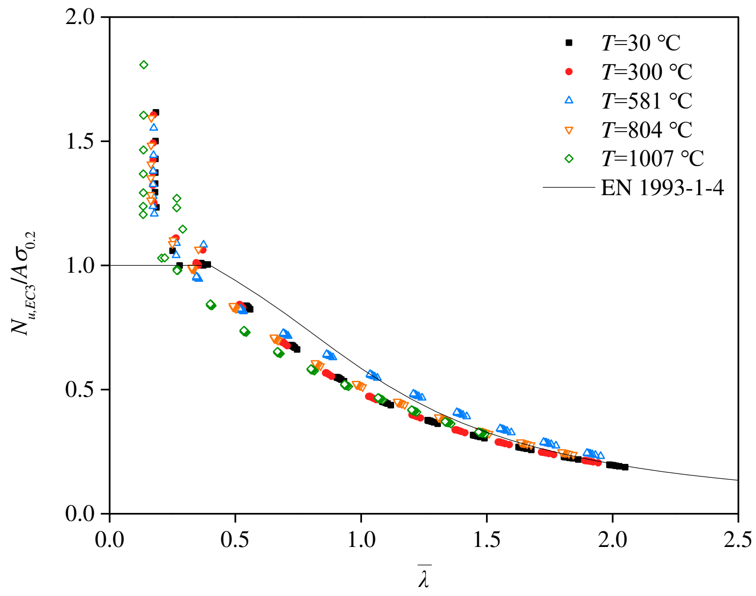

Fig. 11. Comparison of test and numerical failure loads with EC3 design flexural buckling curve.

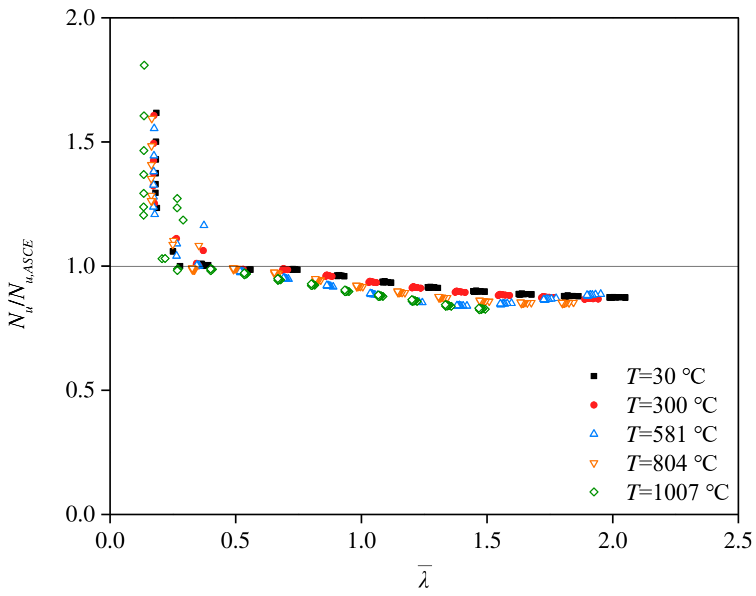

Fig. 12. Comparison of test and numerical failure loads with ASCE flexural buckling strength predictions.

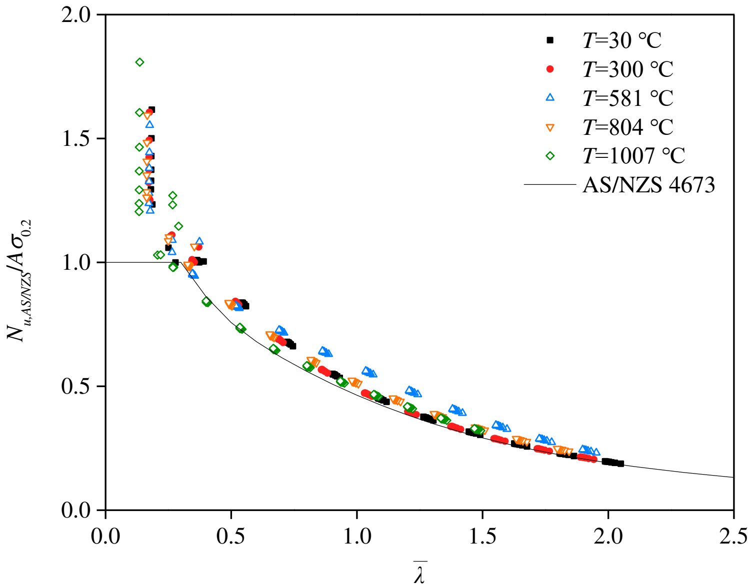

Fig. 13. Comparison of test and numerical failure loads with the AS/NZS design flexural buckling curve.